PERFECTLY-MATCHED-LAYER BOUNDARY INTEGRAL EQUATION METHOD FOR WAVE SCATTERING IN A LAYERED MEDIUM *

WANGTAO LU †, YA YAN LU ‡, AND JIANLIANG QIAN §

Abstract. For scattering problems of time-harmonic waves, the boundary integral equation (BIE) methods are highly competitive, since they are formulated on lower-dimension boundaries or interfaces and can automatically satisfy outgoing radiation conditions. For scattering problems in a layered medium, standard BIE methods based on the Green's function of the background medium need to evaluate the expensive Sommerfeld integrals. Alternative BIE methods based on the free-space Green's function give rise to integral equations on unbounded interfaces which are not easy to truncate, since the wave fields on these interfaces decay very slowly. We develop a BIE method based on the perfectly matched layer (PML) technique. The PMLs are widely used to suppress outgoing waves in numerical methods that directly discretize the physical space. Our PML-based BIE method uses the PML-transformed free-space Green's function to define the boundary integral operators. The method is efficient, since the PML-transformed free-space Green's function is easy to evaluate and the PMLs are very effective in truncating the unbounded interfaces. Numerical examples are presented to validate our method and demonstrate its accuracy.

1. Introduction. Scattering problems for sound, electromagnetic and elastic waves in layered media are highly relevant for practical applications [11]. Numerical methods that directly discretize the physical domain, such as the finite element method (FEM) [26], are versatile and widely used, but they become too expensive when the scatterer is large compared with the wavelength. The boundary integral equation (BIE) methods [13] are applicable to structures with piecewise constant material parameters. These methods take care of the outgoing radiation condition automatically and reduce the dimension by one, since the integral equations are formulated on material interfaces or boundaries of obstacles. For many problems, BIE methods can outperform FEM and other domain-discretization methods, and deliver highly accurate solutions with relatively reasonable computing efforts.

For scattering problems in a layered medium, the common BIE methods are based on the Green's function of the layered background medium [32, 34, 39], so that the integral equations are formulated on strictly local interfaces or boundaries. However, it is well known that this approach is bottlenecked by the evaluation of Sommerfeld integrals arising from the layered-medium Green's function and its derivatives. Over the past decades, many methods such as high-frequency asymptotics, rational approximations, contour deformations [7, 8, 29, 30, 31], complex images [28, 36, 37], and the steepest descent method [14, 15], have been developed to speed up the computation of Sommerfeld integrals. A detailed discussion on computational cost for evaluating the Sommerfeld integrals can be found in [6].

An alternative approach is to use the free-space Green's function, but then the

*Submitted to the editors 01/19/2017.

Funding: W. Lu is partially supported by the Hundred Talents Program of Zhejiang University and by the National Thousand Young Talents Program, China. Y. Y. Lu is partially supported by the Research Grants Council of Hong Kong Special Administrative Region, China (Grant No. CityU 11301914). J. Qian is partially supported by NSF grants 1522249 and 1614566.

†School of Mathematical Sciences, Zhejiang University, Hangzhou, Zhejiang 310027, China. (wangtaolu@zju.edu.cn)

‡Department of Mathematics, City University of Hong Kong, Kowloon, Hong Kong. (mayylu@cityu.edu.hk)

§Department of Mathematics, Michigan State University, East Lansing, MI 48824, USA. (qian@math.msu.edu)

integral equations must also be formulated on the unbounded interfaces separating different layers of the background medium. Various types of compactly supported functions can be used to truncate the unbounded interfaces and to suppress the artificial reflections from the edges of the truncated sections. Existing methods in this category include the approximate truncation method [24, 33], the taper function method [40, 35, 25], and the windowing function method [4, 27, 5, 20]. In particular, the windowing function method [5] can largely eliminate the artificial reflections, since the errors decrease super-algebraically as the window size is increased. Similar good performance can be observed in [20] that combines windowed layer potentials (in physical space) with a Sommerfeld-type correction (in Fourier space) for scattering problems where the obstacles are close to or even cut through the interfaces of the background layered medium.

In this paper, we develop a BIE method based on perfectly matched layers (PMLs) for two-dimensional (2D) scattering problems in layered media. The PML technique is widely used for domain truncations in wave propagation problems [3, 12]. It can be regarded as a complex coordinate stretching that replaces real independent variables in the original governing equation by complex independent variables, so that the outgoing waves are damped as they propagate into the PML region. Similar to those BIE methods based on the free-space Green's function, our BIE method avoids evaluating expensive Sommerfeld integrals by formulating integral equations along the interfaces of the background layered medium. But instead of the free-space Green's function, we use the PML-transformed free-space Green's function, so that the truncation of the interfaces follows automatically from the truncation of PMLs. Notice that the PML-transformed free-space Green's function can be simply obtained by extending the argument of the usual Green's function to complex space following the definition of the complex square root function.

We implement our PML-based BIE method for 2D scattering problems involving two homogeneous media separated by a single interface. The interface is flat except in a finite section which is referred to as the local perturbation. Additional obstacles are also allowed in the homogeneous media. Two common types of incident waves are considered: a plane incident wave and a cylindrical wave due to a point source. The integral equations are established for a scattered wave satisfying the following radiation condition at infinity: the scattered wave consists of outgoing plane waves and evanescent waves [17, 9, 2]. The scattered wave is defined as the difference between the total wave field and a reference wave field obtained from the same incident wave for the layered background medium (without the local perturbation of the interface and the obstacles).

BIE methods for scattering problems use many different formulations. Some of these formulations are more appropriate for large (i.e. high-frequency) problems, since they give rise to linear systems with better condition numbers which are amenable to iterative methods. Since our purpose is to demonstrate the effectiveness of PML-based BIEs for truncating unbounded interfaces, we adopt a BIE formulation that comes from the Green's representation theorem directly. In addition, we calculate the so-called Neumann-to-Dirichlet (NtD) map (mapping Neumann data to Dirichlet data on the boundary) for each subdomain with constant material parameters, so that the final linear system on interfaces or boundaries of the obstacles can be written down in a very simple form.

To numerically approximate the integral equations, we utilize a graded mesh technique [13], a high-order quadrature rule by Alpert [1], and a novel stabilizing technique. Numerical results indicate that our method is highly accurate and the

truncation of the unbounded interfaces by PML is effective. Typically, for a PML with a thickness of one wavelength and discretized in the same way as discretizing physical space, about seven significant digits can be obtained. Numerical results incidate that if the error is dominated by the truncation of the domain, it decays exponentially when the strength of the PML is increased.

The rest of this paper is organized as follows. In sections 2 and 3, we present our PML-based BIE formulation for solving scattering problems in a layered media. Numerical schemes for discretizing the integral equations are given in section 4. Numerical examples are presented in section 5 to illustrate the performance of our method, and we conclude the paper in section 6.

2. Problem formulation. We focus on layered-medium scattering problems in two dimensions. As shown in Figure 1, the layered medium is x_3-invariant and

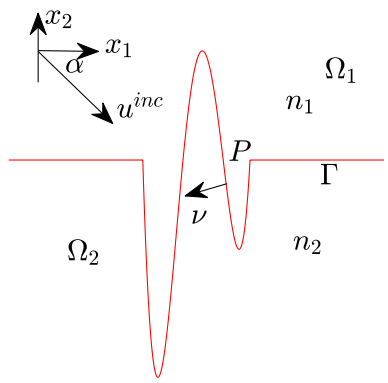

Fig. 1: Profile of a 2D layered medium.

consists of two homogeneous Lipschitz domains Ω_1 and Ω_2 with constant refractive index n_1 and n_2, respectively. The interface Γ on $x_2 = 0$, separates Ω_1 and Ω_2 and contains a local perturbation curve P. Throughout this paper, we assume that the Lipschitz boundary Γ is piecewise analytic and contains a finite number of corners. Here, (x_1, x_2, x_3) denotes the standard Cartesian coordinate system.

Let u^{inc} be an incident wave from the upper medium Ω_1. The total wave field u^{tot}, representing the x_3-component of the electric field in the TE polarization or the x_3-component of the magnetic field in the TM polarization, solves

$$\Delta u^{tot} + k_0^2 n_j^2 u^{tot} = 0, \quad \text{in} \quad \Omega_j, \tag{1}$$

$$[u^{tot}] = 0, \quad \left[\frac{\eta_j \partial u^{tot}}{\partial \boldsymbol{\nu}}\right] = 0, \quad \text{on} \quad \Gamma, \tag{2}$$

where $k_0 = \frac{2\pi}{\lambda}$ is the free-space wavenumber, λ is the wavelength, $\boldsymbol{\nu}$ denotes the unit normal vector along Γ pointing toward Ω_2, $[f]$ denotes the jump of the quantity f across Γ, $\eta_j = 1$ in the TE polarization and $\eta_j = \frac{1}{n_j^2}$ in the TM polarization.

In this paper, we consider two cases of incident waves: a plane wave and a cylindrical wave due to a source at $x^* = (x_1^*, x_2^*) \in \Omega_1$. In the latter case, equation (1)

should be replaced by

$$\Delta u^{tot} + k_0^2 n_j^2 u^{tot} = -\delta(x, x^*), \quad \text{in} \quad \Omega_j, \tag{3}$$

so that u^{tot} represents the layered-medium Green's function excited by the source at x^*. Our scattering problem is to solve (1) and (2) for u^{tot}, subject to the following radiation condition at infinity: u^{tot} is the sum of a known reference wave field u_0^{tot}, and a scattered wave field $u^s := u^{tot} - u_0^{tot}$ that consists of outgoing plane waves and evanescent plane waves both above and below Γ; see the angular spectrum representation [17] and see also the equivalent upward propagating radiation condition [9, 2].

For the case of plane incident waves, suppose $u^{inc} = e^{ik_0 n_1 (x_1 \cos\alpha - x_2 \sin\alpha)}$, where $\alpha \in (0, \pi)$ denotes the angle between the wave direction and the positive x_1-axis. The reference wave field u_0^{tot} is the solution to the scattering problem with the flat interface $x_2 = 0$ and with the same incident wave u^{inc}. It is easy to get that

$$u_0^{tot} = \begin{cases} e^{ik_0 n_1 (x_1 \cos\alpha - x_2 \sin\alpha)} + R e^{ik_0 n_1 (x_1 \cos\alpha + x_2 \sin\alpha)}, & \text{in} \quad \Omega_1, \\ (R+1) e^{ik_0 n_1 x_1 \cos\alpha - ik^* x_2}, & \text{in} \quad \Omega_2, \end{cases} \tag{4}$$

where

$$k^* = k_0 \sqrt{n_2^2 - n_1^2 \cos^2\alpha},$$

$$R = \frac{2}{1 + \frac{k^* \eta}{k_0 n_1 \sin\alpha}} - 1,$$

and $\eta = \eta_1/\eta_2$; when $n_2 \le |n_1 \cos\alpha|$, we set $k^* = ik_0 \sqrt{n_1^2 \cos^2\alpha - n_2^2}$. On the other hand, if the incident wave is $u^{inc} = \frac{i}{4} H_0^{(1)}(k_0 n_1 |x - x^*|)$, a cylindrical wave excited by $x^* \in \Omega_1$, then

$$u_0^{tot} = \begin{cases} u^{inc}, & \text{in} \quad \Omega_1, \\ 0, & \text{in} \quad \Omega_2. \end{cases} \tag{5}$$

Instead of directly computing u^{tot}, we choose to compute the scattered wave field u^s, which satisfies the following transmission condition

$$u_1^s|_\Gamma - u_2^s|_\Gamma = -[u_0^{tot}], \tag{6}$$

$$\eta_1 \frac{\partial u_1^s}{\partial \boldsymbol{\nu}}\bigg|_\Gamma - \eta_2 \frac{\partial u_2^s}{\partial \boldsymbol{\nu}}\bigg|_\Gamma = -\left[\eta_j \frac{\partial u_0^{tot}}{\partial \boldsymbol{\nu}}\right], \tag{7}$$

where u_j^s denotes u^s in Ω_j for $j = 1, 2$. Note that outside the perturbation curve P, $[u_0^{tot}]$ and $[\eta_j \partial_{\boldsymbol{\nu}} u_0^{tot}]$ become zero for plane waves, but they are nonzero for cylindrical waves.

In a typical BIE formulation, computing u^s in the x_1x_2-plane can be reduced to computing u_j^s and $\partial_{\boldsymbol{\nu}} u_j^s$ on the interface Γ only. To solve the governing equations (6) and (7), we require further relations between u_j^s and $\partial_{\boldsymbol{\nu}} u_j^s$ for $j = 1, 2$. Suppose under certain regularity condition, the Neumann-to-Dirichlet (NtD) map $\mathcal{N}_j$, mapping $\partial_{\boldsymbol{\nu}} u_j^s$ to u_j^s on the interface Γ, exists, then, (6) and (7) become

$$\begin{bmatrix} \mathcal{N}_1 & -\mathcal{N}_2 \\ \eta_1 \mathcal{I} & -\eta_2 \mathcal{I} \end{bmatrix} \begin{bmatrix} \partial_{\boldsymbol{\nu}} u_1^s|_\Gamma \\ \partial_{\boldsymbol{\nu}} u_2^s|_\Gamma \end{bmatrix} = \begin{bmatrix} -[u_0^{tot}] \\ -[\eta_j \partial_{\boldsymbol{\nu}} u_0^{tot}] \end{bmatrix}, \tag{8}$$

where $\mathcal{I}$ denotes the identity operator. If the operator matrix on the left-hand side of (8) is invertible, we obtain $\partial_{\boldsymbol{\nu}} u_j^s|_\Gamma$ and then $u_j^s|_\Gamma = \mathcal{N}_s^j \partial_{\boldsymbol{\nu}} u_j^s|_\Gamma$.

In the following, we present a PML-based BIE formulation to solve the problem (8) after a truncation of Γ.

3. NtD map on interface of a PML truncation. Without loss of generality, we consider only the upper homogeneous domain Ω_1, and we will suppress the subscript 1 indexing the domain Ω_1 so that we use Ω, u^s, and n to denote Ω_1, u_1^s, and n_1, respectively.

3.1. Direct truncation. As shown in Figure 2(a), we place a box bounded

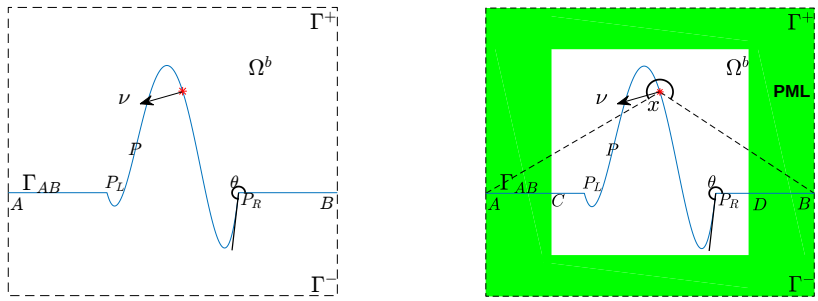

(a) (b)

Fig. 2: Two truncation approaches: (a) direct truncation; (b) PML truncation.

by $\Gamma^+ \cup \Gamma^-$ to enclose P and to truncate the x_1x_2-plane. Then, the interface Γ is truncated to $\Gamma_{AB} = AP_L \cup P \cup P_RB$, while Ω is truncated to a bounded domain Ω^b with the boundary $\Gamma^b = \Gamma_{AB} \cup \Gamma^+$. Existing integral operator theories give the following proposition.

PROPOSITION 1. *In the bounded Lipschitz domain Ω^b, we have:*
(a) Let $g \in H^{-1/2+\delta}(\Gamma^b)$ for $0 < \delta < 1/2$. If $u^s \in H^{1+\delta}(\Omega^b)(\subset C^{0,\delta}(\overline{\Omega^b})$, a Hölder continuous function of order δ) solves

$$\begin{cases} \Delta u^s + k_0^2 n^2 u^s = 0, & \text{in} \quad \Omega^b, \\ \partial_{\boldsymbol{\nu}} u^s = g, & \text{on} \quad \Gamma^b, \end{cases} \tag{9}$$

where $\boldsymbol{\nu}$ denotes the exterior unit normal vector, we have the following representation formula

$$u^s(x) = \int_{\Gamma^b} \{G(x,y)\partial_{\boldsymbol{\nu}} u^s(y) - \partial_{\boldsymbol{\nu}} G(x,y) u^s(y)\} ds(y), \tag{10}$$

for $x \in \Omega^b$, where $G(x,y) = \frac{i}{4} H_0^{(1)}(k_0 n|x-y|)$ is the Green's function of the Helmholtz equation in (9). As x approaches Γ^b, (10) becomes

$$(\mathcal{K} + \mathcal{I})(u^s)(x) = \mathcal{S}(\partial_{\boldsymbol{\nu}} u^s)(x), \tag{11}$$

for a.e. $x \in \Gamma^b$, where the boundary integral operators $\mathcal{K}$ and $\mathcal{S}$ are defined as

$$\mathcal{S}(\phi)(x) = 2\int_{\Gamma^b} G(x,y)\phi(y) ds(y), \tag{12}$$

$$\mathcal{K}(\phi)(x) = 2 \fint_{\Gamma^b} \partial_{\boldsymbol{\nu}} G(x,y)\phi(y) ds(y), \tag{13}$$

and $\fint$ denotes the Cauchy principal integral.
(b) The operator $\mathcal{K} + \mathcal{I}$: $H^{1/2+\delta}(\Gamma^b) \to H^{1/2+\delta}(\Gamma^b)$ is Fredholm of index zero.

Proof. (a). Equation (10) follows from Theorem 7.7 in [23, P. 229]. Equation (11) follows from the jumping conditions in equation (7.5) in [23, P. 218].

(b). We now consider the operator

$$\mathcal{K} + \mathcal{I} = \mathcal{K} - \mathcal{K}_0 + \mathcal{K}_0 + \mathcal{I},$$

where we define

$$\mathcal{K}_0(\phi)(x) = 2 \fint_{\Gamma^b} \partial_{\boldsymbol{\nu}} G_0(x,y)\phi(y) ds(y), \tag{14}$$

and $G_0(x,y) = \frac{1}{2\pi}\log|x-y|$ is the Green's function of Laplace operator $-\Delta$. Since $\mathcal{K} - \mathcal{K}_0$ is compact from $H^0(\Gamma^b)$ to $H^1(\Gamma^b)$ [16, Th 4.3], we see from Theorem 3.27 in [23, P. 87] that $\mathcal{K} - \mathcal{K}_0$ is compact from $H^{1/2+\delta}(\Gamma^b)$ to $H^{1/2+\delta}(\Gamma^b)$. Consequently, (b) follows from the fact that $\mathcal{K}_0 + \mathcal{I} : H^{1/2+\delta}(\Gamma^b) \to H^{1/2+\delta}(\Gamma^b)$ is Fredholm of index zero [16, Th 4.4]. ∎

According to Proposition 1, if $k_0^2 n^2$ is not an eigenvalue of problem (9) with $g \equiv 0$ on Γ^b, then $\mathcal{K} + \mathcal{I} : H^{1/2+\delta}(\Gamma^b) \to H^{1/2+\delta}(\Gamma^b)$ is invertible so that the NtD map $\mathcal{N} = (\mathcal{K} + \mathcal{I})^{-1}\mathcal{S}$ mapping from Neumann data $\partial_{\boldsymbol{\nu}} u \in H^{-1/2+\delta}(\Gamma^b)$ to Dirichlet data $u \in H^{1/2+\delta}(\Gamma^b)$ exists.

According to [19, Eq. (6.50)], equation (11) does not hold at the finite number of corners of Γ^b and should be modified to

$$\mathcal{K}(u^s)(x) + \frac{\theta(x)}{\pi} u^s(x) = \mathcal{S}(\partial_{\boldsymbol{\nu}} u^s)(x), \tag{15}$$

so that it holds for all $x \in \Gamma^b$. Here, $\theta(x)$ is defined as the interior angle between the left and right tangents of x on Γ^b that is inside Ω^b; see $\theta(P_R)$ in Figure 2. Moreover, if we set $\phi \equiv 1$ in equation (6.50) in [19], we obtain

$$\mathcal{K}_0(1)(x) = -\frac{\theta(x)}{\pi}, \tag{16}$$

for all $x \in \Gamma^b$. Hence, equation (15) can be rewritten as

$$[\mathcal{K} - \mathcal{K}_0(1)](u^s) = \mathcal{S}(\partial_{\boldsymbol{\nu}} u^s), \tag{17}$$

on Γ^b. In practice, as suggested in [18, P.158] and in [13, Sec. 3.5], $\mathcal{K}_0(1)$ must be numerically evaluated based on the same discretization as for $\mathcal{K}$; directly using its exact value (16) causes pronounced numerical errors in the vicinity of corners which was verified in [22, Sec 6]. Consequently, we prefer defining the NtD map $\mathcal{N}$ as $\mathcal{N} = [\mathcal{K} - \mathcal{K}_0(1)]^{-1}\mathcal{S}$.

To truncate $\mathcal{N}$ onto Γ_{AB} only, a significant question arises: what boundary conditions should we impose on Γ^+? One may directly specify that $u^s \approx 0$ and $\partial_{\boldsymbol{\nu}} u^s \approx 0$ on Γ^+, but this induces a large truncation error as illustrated in [17, Sec IV]. Certainly, we may place Γ^+ farther away from P to reduce the truncation error but this increases the computational burden. To maintain computational efficiency and to reduce the truncation error, we design a PML to make u^s and $\partial_{\boldsymbol{\nu}} u^s$ decay more rapidly, as will be presented below.

3.2. PML truncation. We introduce the complex coordinate stretching function $\tilde{x}(x) = (\tilde{x}_1(x_1), \tilde{x}_2(x_2))$ by defining

$$\tilde{x}_l(x_l) = x_l + i\int_0^{x_l} \sigma_l(t)dt, \tag{18}$$

for $l = 1, 2$, where we take

$$\sigma_l(t) = \sigma_l(-t), \sigma_l = 0 \text{ for } |t| \le a_l, \text{ and } \sigma_l(t) > 0 \text{ for } |t| > a_l, \tag{19}$$

and $a_1, a_2 > 0$ are such that $[-a_1, a_1] \times [-a_2, a_2]$ encloses the perturbation curve P. Domains with nonzero σ_l are called the *perfectly matched layer* (PML) [3, 12]; see the shaded region shown in Figure 2 (b). Then, we choose $[-a_1 - T, a_1 + T] \times [-a_2 - T, a_2 + T]$ as the box in the previous section to truncate the x_1x_2-plane, where $T > 0$ denotes the thickness of the PML in Ω^b.

In principle, σ_l can be any positive function in the PML region for $|t| > a_l$, e.g., a constant function used in [10]. However, discontinuities of σ_j lead to artificial corners on Γ_{AB} which are not preferred in our BIE formulation, since otherwise the mesh points to be constructed on Γ_{AB} will partly cluster at $|t| = a_l$, which brings in an unnecessary risk of numerical instability as will be illustrated in section 4.2. Thus, we enforce σ_j being sufficiently smooth in the domain Ω^b. Taking σ_1 as an example, its derivatives should vanish at C and D up to a desired order; here, we make use of a scaling function, similar to the function w in [13, Eq. (3.104)], to define σ_1. Specifically, we take

$$\sigma_1(x_1) = \begin{cases} \frac{2Sf_1^p}{f_1^p + f_2^p}, & a_1 \le x_1 \le a_1 + T, \\ S, & x_1 > a_1 + T, \\ \sigma_1(-x_1), & x_1 \le -a_1, \end{cases} \tag{20}$$

where p is a positive integer,

$$f_1 = \left(\frac{1}{2} - \frac{1}{p}\right)\bar{x}_1^3 + \frac{\bar{x}_1}{p} + \frac{1}{2}, \quad f_2 = 1 - f_1, \quad \bar{x}_1 = \frac{x_1 - (a_1 + T)}{T},$$

and $S > 0$ determines the magnitude of σ_1 so that it can be used to adjust the PML strength for absorbing a scattered wave [12]. It is not hard to show that σ_1 maps $[a_1, a_1 + T]$ onto $[0, S]$, and its derivatives vanish at $x_1 = \pm a_1$ up to order p. Figure 3 displays the graph of $\sigma_1(x_1)$ used in Example 1 of section 5, where we set $a_1 = T = 1$, $S = 2$ and $p = 6$. One similarly defines σ_2.

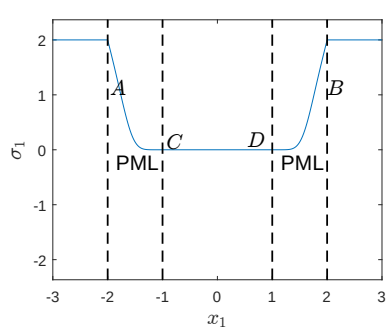

Fig. 3: A typical profile of σ_1.

Using the Green's representation formula (10), we can analytically continue u^s in the domain $\tilde{\Omega}^b = \{\tilde{x}(x)|x \in \Omega^b\}$ by defining, for $\tilde{x} \in \tilde{\Omega}^b$,

$$u^s(\tilde{x}) = \int_{\Gamma^b} \{G(\tilde{x}, y)\partial_{\boldsymbol{\nu}} u^s(y) - \partial_{\boldsymbol{\nu}} G(\tilde{x}, y) u^s(y)\} dy. \tag{21}$$

According to [21, Lem. 2.3], $u^s(\tilde{x})$ satisfies

$$\tilde{\Delta} u^s(\tilde{x}) + k_0^2 n^2 u^s(\tilde{x}) = 0, \tag{22}$$

in $\tilde{\Omega}^b$, where $\tilde{\Delta} = \partial^2_{\tilde{x}_1} + \partial^2_{\tilde{x}_2}$. Defining the complexified function $\tilde{u}^s(x) = u^s(\tilde{x})$ on Ω^b, we see that equation (22) can be rewritten by the chain rule as

$$\nabla \cdot (\mathbf{A} \nabla \tilde{u}^s) + k_0^2 n^2 J \tilde{u}^s = 0, \tag{23}$$

where $\alpha_1(x_1) = 1 + i\sigma_1(x_1)$, $\alpha_2(x_2) = 1 + i\sigma_2(x_2)$, $\mathbf{A} = \mathrm{diag}\{\alpha_2/\alpha_1, \alpha_1/\alpha_2\}$, and $J(x) = \alpha_1(x_1)\alpha_2(x_2)$.

As shown in [21, Th 2.8], the fundamental solution to (23), which we call the PML-transformed free-space Green's function, is

$$\tilde{G}(x, y) = G(\tilde{x}, \tilde{y}) = \frac{i}{4} H_0^{(1)}(k_0 n \rho(\tilde{x}, \tilde{y})), \tag{24}$$

where the complexified distance function ρ is defined to be

$$\rho(\tilde{x}, \tilde{y}) = [(\tilde{x}_1 - \tilde{y}_1)^2 + (\tilde{x}_2 - \tilde{y}_2)^2]^{1/2}, \tag{25}$$

and the half-power operator $z^{1/2}$ is chosen to be the branch of $\sqrt{z}$ with nonnegative real part for $z \in \mathbb{C} \backslash (-\infty, 0]$. Then, we have the following proposition.

Proposition 2. *Let $g \in H^{-1/2+\delta}(\Gamma^b)$ for $0 < \delta < 1/2$. If $\tilde{u}^s \in H^{1+\delta}(\Omega^b)$ solves*

$$\begin{cases} \nabla \cdot (\mathbf{A} \nabla \tilde{u}^s) + k_0^2 n^2 J \tilde{u}^s = 0, & \text{in} \quad \Omega^b, \\ \partial_{\boldsymbol{\nu}_c} \tilde{u}^s = g, & \text{on} \quad \Gamma^b, \end{cases} \tag{26}$$

where $\boldsymbol{\nu}_c = \mathbf{A}^T \boldsymbol{\nu}$ and $\partial_{\boldsymbol{\nu}_c} = \boldsymbol{\nu}_c \cdot \nabla$, the trace $\tilde{u}^s|_{\Gamma^b} \in H^{1/2+\delta}(\Gamma^b)$ and $\partial_{\boldsymbol{\nu}_c} u^s|_{\Gamma^b} \in H^{-1/2+\delta}(\Gamma^b)$ then satisfy the integral representation

$$\tilde{u}^s(x) = \int_{\Gamma^b} \{\tilde{G}(x, y)\partial_{\boldsymbol{\nu}_c} \tilde{u}^s(y) - \partial_{\boldsymbol{\nu}_c} \tilde{G}(x, y) \tilde{u}^s(y)\} ds(y), \tag{27}$$

for all $x \in \Omega^b$. Moreover, as x approaches Γ^b,

$$(\tilde{\mathcal{K}} + \mathcal{I})(\tilde{u}^s)(x) = \tilde{\mathcal{S}}(\partial_{\boldsymbol{\nu}_c} \tilde{u}^s)(x), \tag{28}$$

for a.e. $x \in \Gamma^b$. Here, the integral operators $\tilde{\mathcal{S}}$ and $\tilde{\mathcal{K}}$ are defined by (12) and (13) with G replaced by $\tilde{G}$ and $\boldsymbol{\nu}$ replaced by $\boldsymbol{\nu}_c$, respectively.

Proof. The proof is the same as Proposition 1(a) since the complexified Helmholtz equation in (26) is still strongly elliptic. ∎

Like equation (11), equation (28) should also be modified at corners. In fact, we have

$$\tilde{\mathcal{K}}(\tilde{u}^s)(x) - \tilde{\mathcal{K}}_0(1)\tilde{u}^s(x) = \tilde{\mathcal{S}}(\partial_{\boldsymbol{\nu}_c} \tilde{u}^s)(x), \tag{29}$$

for all $x \in \Gamma^b$, where $\tilde{\mathcal{K}}_0$ is defined as $\tilde{\mathcal{K}}$ but with $\tilde{G}(x,y)$ replaced by

$$\tilde{G}_0(x,y) = -\frac{1}{2\pi}\log\rho(\tilde{x},\tilde{y}), \tag{30}$$

which is the Green's function of the complexified Laplace equation

$$\nabla\cdot(\mathbf{A}\nabla\tilde{u}_0(x)) = 0. \tag{31}$$

The derivation is as follows. Setting $k_0 = 0$ and $\tilde{u}^s = 1$ in (27) so that $\tilde{G}$ is replaced by $\tilde{G}_0$, we obtain

$$1 = \int_{\Gamma^b}\{-\partial_{\boldsymbol{\nu}_c}\tilde{G}_0(x,y)\}ds(y). \tag{32}$$

Then, (27)$-\tilde{u}^s(x)\times$(32) gives

$$\begin{aligned}&\int_{\Gamma^b}\partial_{\boldsymbol{\nu}_c}(\tilde{G}-\tilde{G}_0)(x,y)\tilde{u}^s(y)ds(y) + \int_{\Gamma^b}\partial_{\boldsymbol{\nu}_c}\tilde{G}_0(x,y)(\tilde{u}^s(y)-\tilde{u}^s(x))ds(y)\\ &= \int_{\Gamma^b}\tilde{G}(x,y)\partial_{\boldsymbol{\nu}_c}\tilde{u}^s(y)ds(y).\end{aligned} \tag{33}$$

Consequently, equation (29) follows from the fact that both

$$\partial_{\boldsymbol{\nu}_c}(\tilde{G}-\tilde{G}_0)(x,y) \text{ and } \partial_{\boldsymbol{\nu}_c}\tilde{G}_0(x,y)(\tilde{u}^s(y)-\tilde{u}^s(x))$$

are weakly singular. As for $\tilde{\mathcal{K}}_0(1)$, we have exactly the same formula as (16) due to the following proposition.

PROPOSITION 3. *For any $x \in \Gamma^b$, we have*

$$\tilde{\mathcal{K}}_0(1)(x) = -\frac{\theta(x)}{\pi}. \tag{34}$$

Proof. At first, using the Green's identity, we easily see that

$$\tilde{\mathcal{K}}_0(1)(x) = \lim_{r\to 0+} 2\int_{\partial B(x,r)\cap\overline{\Omega^b}}\partial_{\boldsymbol{\nu}_c}G_0(x,y)ds(y), \tag{35}$$

where $\partial B(x,r)$ is a circle of radius r centered at x, and here the unit normal vector $\boldsymbol{\nu}$ points toward Ω^b.

For a sufficiently small r, one can parameterize $\partial B(x,r)\cap\overline{\Omega^b}$ by $y = x + r(\cos t, \sin t)$ for $t \in [\theta_1,\theta_2]$ so that the interior angle $\theta = \theta_2 - \theta_1$. Thus, equation (35) becomes

$$\tilde{\mathcal{K}}_0(1)(x) = -\frac{1}{\pi}\lim_{y\to 0+}\int_{\theta_1}^{\theta_2}\frac{(\tilde{y}_1-\tilde{x}_1)\tilde{y}_2' - \tilde{y}_1'(\tilde{y}_2-\tilde{x}_2)}{|\tilde{x}-\tilde{y}|^2}dt. \tag{36}$$

By (18), we have

$$\tilde{y}_j - \tilde{x}_j = \int_{x_j}^{y_j}\alpha_j(s)ds = \int_{x_j}^{x_j+r\cos t}\alpha_j(s)ds = \alpha_j(x_j)r\cos t + O(r^2), \tag{37}$$

for $j = 1, 2$. Thus,

$$\begin{aligned}\tilde{\mathcal{K}}_0(1)(x) &= -\frac{1}{\pi}\lim_{r\to 0+}\int_{\theta_1}^{\theta_2}\frac{\alpha_1(x_1)\alpha_2(x_2)r^2 + O(r^3)}{\alpha_1^2(x_1)r^2\cos^2 t + \alpha_2^2(x_2)r^2\sin^2 t + O(r^3)}dt \\ &= -\frac{1}{\pi}\int_{\theta_1}^{\theta_2}\frac{\alpha_1(x_1)\alpha_2(x_2)}{\alpha_1^2(x_1)\cos^2 t + \alpha_2^2(x_2)\sin^2 t}dt \\ &= -\frac{1}{\pi}\int_{\theta_1}^{\theta_2} d(\arctan(\alpha_2/\alpha_1\tan t)). \end{aligned} \tag{38}$$

If x is outside the PML so that $\alpha_1(x) = \alpha_2(x) = 1$, then

$$\tilde{\mathcal{K}}_0(1)(x) = -\frac{\theta_2 - \theta_1}{\pi} = -\frac{\theta}{\pi}.$$

When x is inside the PML, one can easily verify (34) on each part of Γ^b. For example, if x is a smooth point of Γ_{AB}, one sets $\theta_1 = 0$ and $\theta_2 = \pi$ so that $\theta = \pi$. Thus,

$$\tilde{\mathcal{K}}_0(1)(x) = -\frac{1}{\pi}\left(\int_0^{\pi/2} + \int_{\pi/2}^{\pi} d(\arctan(\alpha_2/\alpha_1\tan t))\right) = -\frac{\pi}{\pi}. \tag{39}$$

If x is at the vertex A, then one sets $\theta_1 = 0$ and $\theta_2 = \frac{\pi}{2}$ so that we obtain $\tilde{\mathcal{K}}_0(1)(A) = -\frac{\pi/2}{\pi}$, etc. ∎

In practice, through the use of equation (29), we define the PML-transformed NtD map as $\tilde{\mathcal{N}} = (\tilde{\mathcal{K}} - \tilde{\mathcal{K}}_0(1))^{-1}\tilde{\mathcal{S}}$, which maps $\partial_{\boldsymbol{\nu}_c}\tilde{u}^s$ to $\tilde{u}^s$ on Γ^b; the invertibility of $\tilde{\mathcal{K}} - \tilde{\mathcal{K}}_0(1)$ is under investigation. Analogous to $\mathcal{K}_0(1)$, we need to numerically evaluate $\tilde{\mathcal{K}}_0(1)$.

3.3. Truncation of $\tilde{\mathcal{N}}$ onto Γ_{AB}. According to the radiation condition, u^s is a superposition of outgoing plane waves and evanescent waves, but any outgoing plane wave becomes evanescent in the PML so that $\tilde{u}^s$ in the PML becomes a superposition of evanescent waves only. Thus, we expect that $\tilde{u}^s$ and $\partial_{\boldsymbol{\nu}_c}\tilde{u}^s$ decay to zero more rapidly than u^s and $\partial_{\boldsymbol{\nu}}u^s$ so that it is more accurate to approximate $\tilde{u}^s \approx 0$ and $\partial_{\boldsymbol{\nu}_c}\tilde{u}^s \approx 0$ on Γ^+. Therefore, operators $\tilde{\mathcal{K}}$ and $\tilde{\mathcal{S}}$ in (28) can be truncated onto the truncated interface Γ_{AB} only; in other words,

$$\tilde{\mathcal{K}}_{AB}(\tilde{u}^s)(x) - \tilde{\mathcal{K}}_0(1)(x)\tilde{u}^s(x) \approx \tilde{\mathcal{S}}_{AB}(\partial_{\boldsymbol{\nu}_c}\tilde{u}^s)(x), \tag{40}$$

for $x \in \Gamma_{AB}$, where the definition of $\tilde{\mathcal{S}}_{AB}$ is the same as $\tilde{\mathcal{S}}$ but with the integral domain replaced by Γ_{AB}, etc.

As for $\tilde{\mathcal{K}}_0(1)$, we need to remove the integration domain Γ^+ so that only Γ_{AB} is involved. According to [22, Sec 8], one easily verifies that if x is neither A nor B,

$$\tilde{\mathcal{K}}_0(1)(x) = \mathcal{K}_0(1)(x) = -\angle AxB/\pi + \mathcal{K}_{0,AB}(1)(x), \tag{41}$$

where $\angle AxB$ denotes the angle between and above the two segments Ax and xB (see Fig. 2(b)), and $\mathcal{K}_{0,AB}$ is defined by (14) but with the integration domain replaced by Γ_{AB}; otherwise, we simply set $\tilde{\mathcal{K}}_0(1)(x) = -1$. Therefore, equation (40) becomes

$$\tilde{\mathcal{K}}_{AB}(\tilde{u}^s)(x) + (\angle AxB/\pi - \mathcal{K}_{0,AB}(1)(x))\,\tilde{u}^s(x) \approx \tilde{\mathcal{S}}_{AB}(\partial_{\boldsymbol{\nu}_c}\tilde{u}^s)(x). \tag{42}$$

Consequently, numerically discretizing the involved integral operators in (42) approximates the PML-transformed NtD map $\tilde{\mathcal{N}}$ on Γ_{AB}.

4. Numerical implementation. In this section, we consider the discretization of the integral operators $\tilde{\mathcal{K}}_{AB}$, $\tilde{\mathcal{S}}_{AB}$, and $\mathcal{K}_{0,AB}$ on Γ_{AB}. Suppose the piecewise smooth curve Γ_{AB} is parameterized by $x(s) = \{(x_1(s), x_2(s))|0 \le s \le L\}$, where s is the arclength parameter. Since corners may exist, $\tilde{u}^s$ can have corner singularities in its derivatives at corners. To treat the corner singularities of $\tilde{u}^s$, we follow [13, Sec. 3.5], constructing a graded mesh on Γ_{AB} through the use of a scaling function $s = w(t), 0 \le t \le 1$ so that integrands in (42) vanish at corners up to a certain order. For a smooth segment of Γ_{AB} corresponding to $s \in [s^0, s^1]$ and $t \in [t^0, t^1]$ such that $s^l = w(t^l)$ for $l = 0, 1$, where s^0 and s^1 correspond to two corners, we take [13, Eq. (3.104)]

$$s = w(t) = \frac{s^0 w_1^p + s^1 w_2^p}{w_1^p + w_2^p}, \quad t \in [t^0, t^1], \tag{43}$$

where we recall that p is used in (20) to define σ_1, and

$$w_1 = \left(\frac{1}{2} - \frac{1}{p}\right)\xi^3 + \frac{\xi}{p} + \frac{1}{2}, \quad w_2 = 1 - w_1, \quad \xi = \frac{2t - (t^0 + t^1)}{t^1 - t^0}.$$

One easily verifies that the derivatives of $w(t)$ vanish at the corners up to order p. Assume that $t \in [0, 1]$ is uniformly sampled by an even number, denoted by N, of grid points $\{t_j = jh\}_{j=1}^N$ with grid size $h = 1/N$, and that the grid points contain those corner points. The scaling function $s = w(t)$ creates a graded mesh on Γ_{AB} such that roughly one half of grid points cluster around the corners whereas the other half are nearly equally distributed [13, Sec. 3.5].

To simplify the notations, we use $x(t)$ to denote $x(w(t))$, and $x'(t)$ to denote $\frac{dx}{ds}(w(t))w'(t)$ in the following.

4.1. Approximating $\tilde{\mathcal{N}}$ on Γ_{AB}. According to the definitions, operators $\tilde{\mathcal{S}}_{AB}$ and $\tilde{\mathcal{K}}_{AB}$ at $x = x(t_l)$, $l = 1, \cdots, N$ can be parameterized by

$$\tilde{\mathcal{S}}_{AB}(\partial_{\boldsymbol{\nu}_c}\tilde{u}^s)(x(t_l)) = \int_0^1 \tilde{S}(t_l, t)\phi(t)dt \tag{44}$$

$$\tilde{\mathcal{K}}_{AB}(\tilde{u}^s)(x(t_l)) = \int_0^1 \tilde{K}(t_l, t)\tilde{u}^s(x(t))dt, \tag{45}$$

where $\phi(t) = \partial_{\boldsymbol{\nu}_c}\tilde{u}^s(x(t))|x'(t)|$, $\mathrm{dist}(t_l, t) = \rho(x(t_l), x(t))$, $\kappa(t_l, t) = \tilde{x}_2'(t)(\tilde{x}_1(t) - \tilde{x}_1(t_l)) - \tilde{x}_1'(t)(\tilde{x}_2(t) - \tilde{x}_2(t_l))$, and

$$\tilde{S}(t_l, t) = \frac{i}{2}H_0^{(1)}(k_0 n\ \mathrm{dist}(t_l, t)) \tag{46}$$

$$\tilde{K}(t_l, t) = -\frac{ik_0 n}{2}\frac{\kappa(t_l, t)}{\mathrm{dist}(t_l, t)}H_1^{(1)}(k_0 n \mathrm{dist}(t_l, t)). \tag{47}$$

The integrands in (44) and (45) have logarithmic singularities at $t = t_l$. To discretize such integrals, a common approach is to use the kernel splitting technique introduced in [13, Sec 3.5], but this fails here. Taking $\tilde{S}_{AB}$ as an example, this technique requires the decomposition

$$\tilde{S}(t_l, t) = \tilde{S}_1(t_l, t)\log(4\sin^2(\pi(t_l - t)) + \tilde{S}_2(t_l, t),$$

where

$$\tilde{S}_1(t_l, t) = -\frac{1}{2\pi}J_0(k_0 n\ \mathrm{dist}(t_l, t)), \tag{48}$$

and $\tilde{S}_2$ are analytic for $t \in [0,1]$. In the PML region, the Bessel function J_0 blows up quickly towards infinity since $\mathrm{dist}(t_l, t)$ is no longer real and may have significant imaginary part.

Nevertheless, this can be simply remedied by Alpert's hybrid Gauss-trapezoidal quadrature rule [1], which does not perform kernel splittings. Following this approach, we discretize the integral in (44) as

$$\begin{aligned}\tilde{\mathcal{S}}_{AB}(\partial_{\boldsymbol{\nu}_c}\tilde{u}^s)(x(t_l)) \approx \sum_{k=1}^{K_1}\gamma_k h[&\tilde{S}(t_l, t_l+\delta_k h)\phi(t_l+\delta_k h)\\ &+\tilde{S}(t_l, t_l+1-\delta_k h)\phi(t_l+1-\delta_k h)]\\ &+\sum_{k=K_2}^{N-K_2} h\tilde{S}(t_l, t_l+t_k)\phi(t_l+t_k),\end{aligned} \tag{49}$$

where values of K_1, K_2, γ_k, and δ_k depend on the order of Alpert's quadrature rule and can be precomputed. For example, in a sixth order quadrature formula, we have $K_1 = 5$ and $K_2 = 3$; the associated $\{\delta_k, \gamma_k\}_{k=1}^5$ are given in Table 1; please see [1] for details.

k	δ_k	γ_k
1	4.00488 41949 26570 E-03	1.67187 96911 47102 E-02
2	7.74565 53733 36686 E-02	1.63695 83714 47360 E-01
3	3.97284 99935 23248 E-01	4.98185 65697 70637 E-01
4	1.07567 33529 15104 E+00	8.37226 62455 78912 E-01
5	2.00379 69271 11872 E+00	9.84173 08440 88381 E-01

Table 1: Parameters for the sixth order Alpert's quadrature rule.

By choosing a sufficiently large p, the scaling function $w(t)$ can make the derivatives of $\phi(t)$ to vanish at the corners up to any given order, so that $\phi(t)$ is approximately a smooth periodic function. Therefore, its trigonometric interpolation [38, Eq. (3.8), Th 4.1] can be used to approximate ϕ and attains a high accuracy. Thus, we have

$$\phi(t) \approx \sum_{j=1}^{N} \phi(t_j) L(t - t_j), \tag{50}$$

where $L(t) = \sin(N\pi t)/[N\tan(\pi t)]$ is the Sinc function, satisfying $L(t_j) = 0$ for $1 \le j < N$ and $L(1) = L(0) = 1$. Utilizing (50), we may rewrite equation (49) in terms of $\phi(t_j)$ for $1 \le j \le N$ so that we obtain an $N \times N$ matrix $\tilde{\mathbf{S}}$ that satisfies

$$\tilde{\mathcal{S}}_{AB}(\partial_{\nu_c}\tilde{u}^s)\begin{bmatrix} x(t_1) \\ \vdots \\ x(t_N)\end{bmatrix} \approx \tilde{\mathbf{S}}\begin{bmatrix}\phi(t_1)\\ \vdots \\ \phi(t_N)\end{bmatrix}, \tag{51}$$

where the term on the left-hand side represents a column vector of $\tilde{\mathcal{S}}_{AB}(\partial_{\nu_c}\tilde{u}^s)(x(t_j))$ for $1 \le j \le N$.

Similarly, one obtains the discretization of $\tilde{\mathcal{K}}_{AB}$ as follows,

$$\tilde{\mathcal{K}}_{AB}(\tilde{u}^s)\begin{bmatrix} x(t_1) \\ \vdots \\ x(t_N) \end{bmatrix} \approx \tilde{\mathbf{K}}\begin{bmatrix} \tilde{u}^s(t_1) \\ \vdots \\ \tilde{u}^s(t_N) \end{bmatrix}, \tag{52}$$

where $\tilde{\mathbf{K}}$ represents an $N \times N$ matrix, and so does the discretization of $\mathcal{K}_{0,AB}$.

Thus, collocating (42) at $x(t_l), l = 1, \ldots, N$, yields

$$(\tilde{\mathbf{K}} + \tilde{\mathbf{H}})\tilde{\mathbf{u}}^s \approx \tilde{\mathbf{S}}\boldsymbol{\phi}, \tag{53}$$

where $\tilde{\mathbf{H}}$ is a diagonal matrix with entries $\angle Ax(t_l)B/\pi - \mathcal{K}_{0,AB}(1)(x(t_l))$,

$$\tilde{\mathbf{u}}^s = [\tilde{u}^s(x(t_1)), \ldots, \tilde{u}^s(x(t_N))]^T,$$
$$\boldsymbol{\phi} = [\phi(x(t_l)), \ldots, \phi(x(t_N))]^T.$$

Consequently, one gets

$$\tilde{\mathbf{u}}^s \approx (\tilde{\mathbf{K}} + \tilde{\mathbf{H}})^{-1}\tilde{\mathbf{S}}\boldsymbol{\phi} := \tilde{\mathbf{N}}\boldsymbol{\phi}, \tag{54}$$

where the $N \times N$ matrix $\tilde{\mathbf{N}}$ in fact approximates the scaled PML-transformed NtD map $\tilde{\mathcal{N}}_s$ mapping $\phi = |x'|\partial_{\boldsymbol{\nu}_c}\tilde{u}^s$ to $\tilde{u}^s$ on Γ_{AB}.

4.2. A stabilizing technique. Clearly, to make the approximations of $\tilde{\mathcal{S}}_{AB}$ and $\tilde{\mathcal{K}}_{AB}$ accurate enough, a high order quadrature rule and a large scaling parameter p are always preferred; otherwise, one needs a large N. Suppose we desire sixth order of accuracy so that nodes and weights of Alpert's quadrature rule are chosen based on Table 1. To be consistent, we choose $p = 6$ in the scaling function $s = w(t)$. Under such a circumstance, when computing the kernel functions $\tilde{S}(t_l, t)$ and $\tilde{K}(t_l, t)$, we observe that $|t_l - t|$ can be as small as $\delta_1 h = O(\frac{10^{-3}}{N})$. When t_l is close to a corner point, the physical distance $\text{dist}(t_l, t)$ can be further shrunk to $O(\frac{10^{-3p}}{N^p}) = O(\frac{10^{-18}}{N^6})$ by $s = w(t)$. Unfortunately, even for a coarse mesh, this can be less than or close to the round-off error $O(10^{-16}x(t_l))$ in the computation of $\text{dist}(t_l, t)$. In such a situation, $\text{dist}(t_l, t)$ is simply regarded as 0 in a double-precision computation. Consequently, division by zero occurs in the computation of $\tilde{S}(t_l, t)$ and $\tilde{K}(t_l, t)$ when t is close to t_l and when t_l is close to a corner. To resolve this instability issue, one approach is to reduce p to be no more than 3, but this lowers the order of accuracy. Consequently, we develop a stabilizing technique which can provide sufficient significant digits in computing $\tilde{S}(t_l, t)$ and $\tilde{K}(t_l, t)$ in the extreme situation that t is close to t_l, t_l is close to some corner, and p is high.

Observing the definitions (46) and (47), the instability issue comes from the two terms $\text{dist}(t_l, t)$ and $\kappa(t_l, t)$ since they involve subtractions of two extremely close quantities. We discuss $\text{dist}(t_l, t)$ first. Without loss of generality, we assume that $t > t_l$, so that $\tilde{x}(\xi)$, for $\xi \in [t_l, t]$, becomes a piecewise smooth function; note that here $\tilde{x}(\xi)$ may contain the corner. At first, we assume that $\tilde{x}(\xi)$ for $\xi \in [t_l, t]$ is smooth. To preserve enough significant digits, we compute accurately

$$\tilde{x}_i(t) - \tilde{x}_i(t_l), \tag{55}$$

for $i = 1, 2$. To do so, by the Newton-Leibniz formula, we rewrite (55) in the form

$$\tilde{x}_i(t) - \tilde{x}_i(t_l) = \int_0^{\int_{t_l}^t w'(\tau)d\tau} \frac{d\tilde{x}_i}{ds}(w(t_l) + s)ds, \tag{56}$$

for $i = 1, 2$. Such a representation gives rise to significant advantages. Specifically, the integrand in the primary integral is an $O(1)$ quantity so that numerical integrations (e.g., Gaussian quadrature rules) yield accurate results; moreover, we only need the first-order derivative of $\tilde{x}_i$ to obtain accurate results. Consequently, $\mathrm{dist}(t_l, t)$ can be evaluated via

$$\mathrm{dist}(t_l, t) = \sqrt{\sum_{i=1}^{2} \left(\int_0^{\int_{t_l}^{t} w'(\tau)d\tau} \frac{d\tilde{x}_i}{ds}(w(t_l) + s)ds \right)^2}. \tag{57}$$

Next, we discuss the computation of

$$\begin{aligned} \kappa(t_l, t) =& w'(t) \Big[\frac{d\tilde{x}_2}{ds}(w(t)) \left(\tilde{x}_1(w(t)) - \tilde{x}_1(w(t_l)) \right) \\ & - \frac{d\tilde{x}_1}{ds}(w(t)) \left(\tilde{x}_2(w(t)) - \tilde{x}_2(w(t_l)) \right) \Big] \\ :=& w'(t)\bar{\kappa}(t_l, t). \end{aligned} \tag{58}$$

Using the Newton-Leibniz formula, we may rewrite $\bar{\kappa}(t_l, t)$ as

$$\begin{aligned} \bar{\kappa}(t_l, t) = \int_0^{\int_{t_l}^{t} w'(\tau)d\tau} \int_0^{s} \Big[& \frac{d^2\tilde{x}_2}{ds^2}(w(t_l) + s) \frac{d\tilde{x}_1}{ds}(w(t_l) + \eta) \\ & - \frac{d^2\tilde{x}_1}{ds^2}(w(t_l) + s) \frac{d\tilde{x}_2}{ds}(w(t_l) + \eta) \Big] d\eta ds. \end{aligned} \tag{59}$$

Numerical integrations for the above double integrals provide accurate results.

Now, suppose that $\tilde{x}(\xi)$ for $\xi \in [t_l, t]$ contains a corner at $t^* \in (t_l, t)$. Since $\tilde{x}(\xi)$ consists of two smooth segments corresponding to $[t_l, t^*]$ and $[t^*, t]$, respectively, the following splitting

$$\tilde{x}_i(t) - \tilde{x}_i(t_l) = (\tilde{x}_i(t) - \tilde{x}_i(t^*)) + (\tilde{x}_i(t^*) - \tilde{x}_i(t_l)), \tag{60}$$

indicates that the Newton-Leibniz formula is applicable to either term on the right-hand side so that numerical integrations lead to accurate results for $\tilde{x}_i(t) - \tilde{x}_i(t_l)$ and for $\mathrm{dist}(t_l, t)$. One may compute $\kappa(t_l, t)$ similarly; we omit the details here.

4.3. Wave field evaluations. Suppose now in each domain Ω_j, we have obtained an $N \times N$ matrices $\tilde{\mathbf{N}}_j$ to approximate the scaled NtD operator $\tilde{\mathcal{N}}_{s,j}$, mapping $|x'|\partial_{\boldsymbol{\nu}_c}\tilde{u}_j^s$ to $\tilde{u}_j^s$ on Γ_{AB}, for $j = 1, 2$. Then,

$$\tilde{\mathbf{N}}_j \boldsymbol{\phi}_j = \tilde{\mathbf{u}}_j^s, \tag{61}$$

where

$$\begin{aligned} \tilde{\mathbf{u}}_j^s &= [\tilde{u}_j^s(x(t_1)), \ldots, \tilde{u}_j^s(x(t_N))]^T, \\ \boldsymbol{\phi}_j &= [|x'(t_1)|\partial_{\boldsymbol{\nu}_c}\tilde{u}_j^s(x(t_1)), \ldots, |x'(t_N)|\partial_{\boldsymbol{\nu}_c}\tilde{u}_j^s(x(t_N))]^T. \end{aligned}$$

According to the transmission conditions (6) and (7), the complexified outgoing wave $\tilde{u}_j^s$, at the N grid points on Γ_{AB}, satisfies

$$\tilde{\mathbf{u}}_1^s - \tilde{\mathbf{u}}_2^s = \mathbf{b}_1, \tag{62}$$

$$\eta_1 \boldsymbol{\phi}_1 - \eta_2 \boldsymbol{\phi}_2 = \mathbf{b}_2, \tag{63}$$

where

$$\mathbf{b}_1 = [-[\tilde{u}_0^{tot}](x(t_1)), \ldots, -[\tilde{u}_0^{tot}](x(t_N))]^T,$$
$$\mathbf{b}_2 = [-|x'(t_1)|[\eta_j \partial_{\boldsymbol{\nu}_c} \tilde{u}_0^{tot}](x(t_1)), \ldots, -|x'(t_N)|[\eta_j \partial_{\boldsymbol{\nu}_c} \tilde{u}_0^{tot}](x(t_N))]^T.$$

Thus, by (61), we obtain

$$\begin{bmatrix} \tilde{\mathbf{N}}_1 & -\tilde{\mathbf{N}}_2 \\ \eta_1 \mathbf{I} & -\eta_2 \mathbf{I} \end{bmatrix} \begin{bmatrix} \boldsymbol{\phi}_1 \\ \boldsymbol{\phi}_2 \end{bmatrix} = \begin{bmatrix} \mathbf{b}_1 \\ \mathbf{b}_2 \end{bmatrix}, \tag{64}$$

with the solution

$$\boldsymbol{\phi}_1 = (\tilde{\mathbf{N}}_1 - \frac{\eta_1}{\eta_2} \tilde{\mathbf{N}}_2)^{-1} \left(\eta_2^{-1} \tilde{\mathbf{N}}_2 \mathbf{b}_2 + \mathbf{b}_1 \right), \tag{65}$$

$$\boldsymbol{\phi}_2 = \frac{\eta_1}{\eta_2} \boldsymbol{\phi}_1 - \frac{\mathbf{b}_2}{\eta_2}. \tag{66}$$

Consequently, we obtain $\tilde{\mathbf{u}}_j^s = \tilde{\mathbf{N}}_j \boldsymbol{\phi}_j$ on Γ_{AB}.

As for $x \in \Omega_j$, we directly truncate the integration domain in (27) to Γ_{AB} to compute $\tilde{u}_j^s(x)$; that is,

$$\tilde{u}_j^s(x) \approx \int_{\Gamma_{AB}} \{\tilde{G}_j(x,y) \partial_{\boldsymbol{\nu}_c} \tilde{u}_j^s(y) - \partial_{\boldsymbol{\nu}_c} \tilde{G}_j(x,y) \tilde{u}_j^s(y)\} ds(y). \tag{67}$$

After parameterized by the scaling function $s = w(t)$ in (43), the integrand in (67) becomes periodic and smooth enough so that by the trapezoidal rule, we have

$$\tilde{u}_j^s(x) \approx \frac{1}{N} \sum_{l=1}^{N} \Big[\tilde{G}_j(x, x(t_l)) |x'(t_l)| \partial_{\boldsymbol{\nu}_c} \tilde{u}_j^s(x(t_l)) - \partial_{\boldsymbol{\nu}_c} \tilde{G}_j^s(x, x(t_l)) |x'(t_l)| \tilde{u}_j^s(x(t_l)) \Big]. \tag{68}$$

Therefore, we obtain $u_j^s = \tilde{u}_j^s$ so that the total wave field $u^{tot} = u^s + u_0^{tot}$ in the physical domain outside the PML.

5. Numerical examples. In this section, we will carry out several numerical experiments to demonstrate the efficiency of the proposed PML-BIE formulation. In all examples, the physical domain $\Omega_{\text{PHY}} = \{(x_1, x_2) | |x_1| \leq a_1\}$ where we let a_2 in (19) approach infinity since the choice of a_2 does not affect computing $\tilde{u}_j^s$ on Γ_{AB} for $j = 1, 2$. Accordingly, the PML domain $\Omega_{\text{PML}} = \{(x_1, x_2) | a_1 \leq |x_1| \leq a_1 + T, a_1 > 0, T > 0\}$. Therefore, the truncated interface Γ_{AB} consists of physical interface $\Gamma_{\text{PHY}} = \overline{\Omega_{\text{PHY}}} \cap \Gamma_{AB}$ and the PML interface $\Gamma_{\text{PML}} = \overline{\Omega_{\text{PML}}} \cap \Gamma_{AB}$.

To achieve a high-order accuracy, we take $p = 6$ to define σ_1 and the scaling function $w(t)$, and we apply the sixth order Alpert's quadrature rule with parameters defined in Table 1 to discretize the governing BIEs. In all examples, we will take the free-space wavelength $\lambda = 1$ so that $k_0 = 2\pi$, and we will fix the PML thickness $T = \lambda$.

The truncation error induced in (40) depends on how rapidly $\tilde{u}^s$ decays in the PML, especially along the x_1-axis, and this in fact can be controlled by adjusting σ_1 in the PML [12]. By (20), σ_1 is proportional to its parameter S so that we expect

that the truncation error can be suppressed by increasing S; we will see below that for PMLs with a thickness of one wavelength, one can get sufficiently accurate solutions by choosing $S = 2$.

Example 1. In this example, we assume that Γ is just the flat interface $x_2 = 0$. We take $n_1 = 1$ and $n_2 = 2$, and study a cylindrical incident wave excited by the source $x^* = (0, 0.1)$, so that u^{tot} represents the layered Green's function at x^*. This example is used to validate our method, since a closed form of the layered Green's function is available [31].

In the implementation, although Γ is smooth, we set $(0, 0) \in \Gamma$ as an artificial corner. The reason is that the solution can change extremely rapidly at $(0, 0)$ since it is the closest point to the source x^* on Γ. To capture this sharply changing behavior, we need more points near $(0, 0)$, and regarding $(0, 0)$ as an artificial corner is a quick way to realize the purpose. We consider the TM polarization here, and take $a_2 = a_1 = 1$ so that $\overline{\Omega_{\text{PHY}}} = [-1, 1] \times [-1, 1]$.

Taking $N = 400$, we compute $\tilde{u}^{tot}$ and compare it with the exact solution u^{tot}_{exa} on Γ_{AB}, as shown in Figure 4(a), where the dashed lines are used to separate Γ_{PML} and

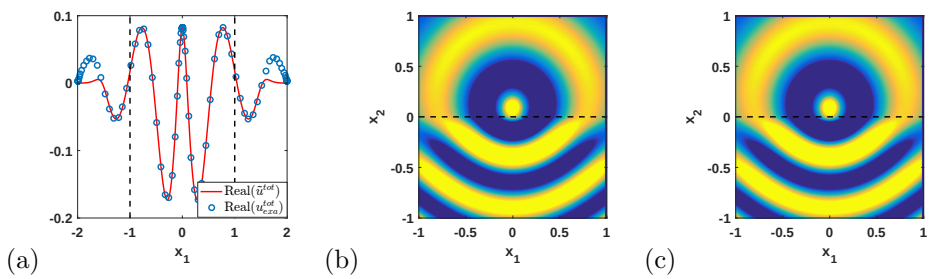

Fig. 4: Example 1: in TM polarization, (a) real parts of $\tilde{u}^{tot}$ and u^{tot}_{exa} on Γ_{AB}; dashed lines separate Γ_{PML} and Γ_{PHY}. Real part of u^{tot} in $\overline{\Omega_{\text{PHY}}}$: (b) numerical solution; (c) exact solution, where dashed lines represent location of Γ.

Γ_{PHY}. We observe that, on Γ_{PHY}, $\tilde{u}^{tot} = u^{tot}$ and u^{tot}_{exa} coincide very well, whereas on Γ_{PML}, $\tilde{u}^{tot}$ decays quickly to 0 and u^{tot}_{exa} keeps oscillating, as what we expected. Figure 4 (b) and (c) show the real part of numerical and exact solutions of u^{tot} in Ω_{PHY}, respectively.

To illustrate that our PML effectively absorbs u^s, we fix $N = 400$ and compute u^{tot} at grid points on Γ_{PHY} for different values of S, ranging from 0.1 to 2; notice that the grid points on Γ_{PHY} are independent of S. Using the exact solution u^{tot}_{exa} as a reference solution, we compute relative errors for different values of S, as shown in Figure 5(a), where only the vertical axis is logarithmically scaled. Those relative errors can somewhat measure the magnitude of the truncation error in (40). We observe that the relative error decays exponentially at the beginning and then yields to the discretization error which dominates the total error when S becomes large.

Next, we study the relative error of u^{tot} on Γ_{PHY} varying the number of grid points N on Γ_{AB} for $S = 2$. Since grid points vary for different values of N, to realize the comparison, we choose to evaluate u^{tot} at the following observation points: the grid points on Γ_{PHY} for $N = 20$; for N greater than 20, we interpolate the numerical solution onto the observation points by (50). Relative errors for different values of N are depicted in Figure 5 (b) with both axes logarithmically scaled. The slope of the

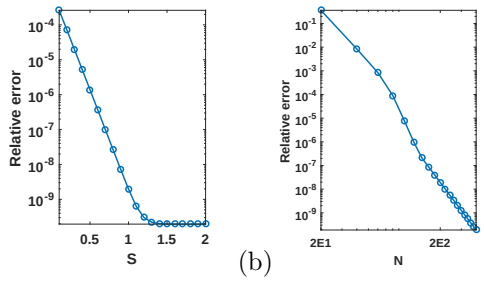

Fig. 5: Example 1: in TM polarization, (a) relative error against S for $N = 400$; (b) relative error against N for $S = 2$.

decreasing part of the curve reveals that our method exhibits at least seventh-order accuracy.

Example 2. We next consider a local perturbation that consists of two connected semicircles of radius 1; the interface is shown as dotted line in Figure 6 (a) and (b). Suppose $n_1 = 1$ and $n_2 = 2$. We consider two different incident waves: a plane wave with the incident angle $\alpha = \frac{\pi}{3}$, and a cylindrical wave excited by the source $x^* = (1, 1)$.

In the implementation, we consider the TE polarization, and take $a_2 = a_1 = 2.5$ so that $\overline{\Omega_{\text{PHY}}} = [-2.5, 2.5] \times [-2.5, 2.5]$. The total wave field u^{tot} for two incident waves in $\overline{\Omega_{\text{PHY}}}$ are plotted in Figure 6 (a) and (b), respectively.

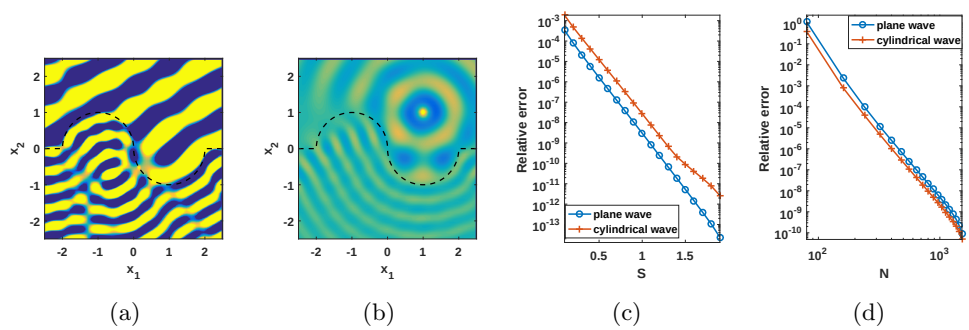

Fig. 6: Example 2: in TE polarization, real part of the wave u^{tot} in $\overline{\Omega_{\text{PHY}}}$: (a) plane incident wave with angle $\alpha = \frac{\pi}{3}$ and (b) cylindrical incident wave with source $\mathbf{x}^* = (1, 1)$, where dashed lines indicate location of Γ. (c): relative error of u^{tot} on Γ_{PHY} against S for $N = 1600$. (d) relative error of u^{tot} on Γ_{PHY} against N for $S = 2$.

Next, we fix $N = 1600$ and compute u^{tot} at grid points on Γ_{PHY} for different values of S, ranging from 0.1 to 2. Taking the numerical solution u^{tot} for $S = 2$ as a reference solution, we compute relative errors for different values of S for both incident waves. Numerical results are shown in Figure 6(c).

At last, we study relative errors of u^{tot} on Γ_{PHY} varying N for $S = 2$. Observation points are chosen as the grid points on Γ_{PHY} for $N = 80$. The reference solution

is obtained by interpolating numerical solution for $N = 1600$ onto the observation points. Numerical results for both incident waves are shown in Figure 6(d).

Example 3. In the third example, we study a more complicated structure, where an obstacle is placed above the interface. With the obstacle involved, our PML-based BIE formulation only requires an extra NtD operator defined on the boundary of the obstacle, which can be computed through the use of (17) [22]. Then, according to transmission conditions on the obstacle and the interface, the final linear system can be obtained by the same procedure.

Suppose $n_1 = 1$, $n_2 = 3$, and the refractive index of the obstacle is $n_{ob} = 2$. The structure is shown in Figure 7, where the interface contains five uniformly spaced indentations and a drop-shaped obstacle is located one unit above the interface. We consider two different incident waves: a plane wave with the incident angle $\alpha = \frac{\pi}{3}$, and a cylindrical wave excited by the source $x^* = (3, 1)$.

In the implementation, we consider the TM polarization and take $a_2 = a_1 = 5.5$ so that $\overline{\Omega_{\text{PHY}}} = [-5.5, 5.5] \times [-5.5, 5.5]$. The total wave field u^{tot} for two incident waves in $\overline{\Omega_{\text{PHY}}}$ are plotted in Figure 7 (a) and (b), respectively.

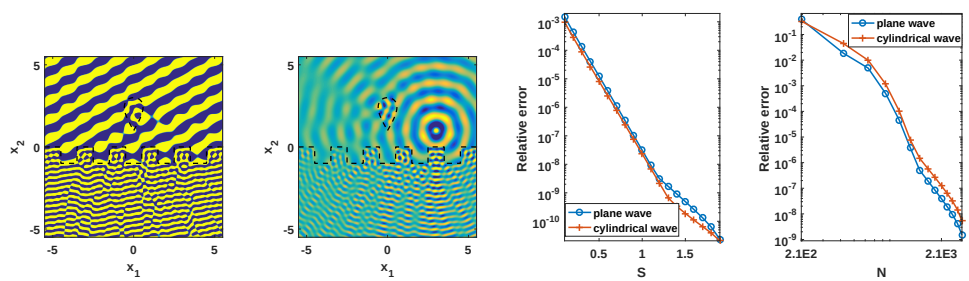

(a) (b) (c) (d)

Fig. 7: Example 3: in TM polarization, real part of u^{tot} in $\overline{\Omega_{\text{PHY}}}$: (a) plane incident wave with angle $\alpha = \frac{\pi}{3}$ and (b) cylindrical incident wave with point source $x^* = (3, 1)$, where dashed line indicates location of Γ. When $N_{ob} = 800$: (c) relative error of u^{tot} on Γ_P against S for $N = 3150$; (d) relative error of u^{tot} on Γ_P against N for $S = 2$.

Taking $N = 3150$ and $N_{ob} = 800$, we next compute u^{tot} at grid points on Γ_{PHY} for S ranging from 0.1 to 2. Taking the numerical solution for $S = 2$ as a reference solution, we compute relative errors for different values of S for both incident waves. Numerical results are shown in Figure 7(c).

At last, we study numerical errors of u^{tot} on Γ_{PHY} varying N when $S = 2$ and $N_{ob} = 800$. Observation points are chosen as the grid points on Γ_{PHY} when $N = 210$. The reference solution is obtained by interpolating the numerical solution for $N = 3150$ onto the observation points. Numerical results for both incident waves are shown in Figure 7(d).

6. Conclusion. For 2D scattering problems in layered media with unbounded interfaces, we developed a PML-based BIE method that relies on the PML-transformed free-space Green's function, which is very easy to evaluate. The method avoids the difficulty of evaluating the expensive Sommerfeld integrals. Similar to other BIE methods based on the free space Green's function, integral equations are formulated

on unbounded interfaces of the background media and these interfaces must be truncated. Unlike existing truncating approaches, the truncation in our method simply follows the well-established PML technique.

Since our main purpose is to develop a PML-based method and demonstrate its effectiveness for truncating the unbounded interfaces, we have used a BIE formulation involving the single- and double-layer boundary integral operators only. In addition, we used the NtD maps to simplify the final linear system. Numerical examples are presented for scattering problems involving two homogeneous media separated by an interface with local perturbations, and possibly with additional obstacles. The integral equations are discretized using a graded mesh technique, Alpert's sixth order hybrid Gauss-trapezoidal rule for logarithmic singularities, and a stabilizing technique. Numerical results indicate that the truncation of interfaces by PML is highly effective. Using PMLs with one-wavelength thickness, we obtained at least seven significant digits in all experiments.

The PML-based BIE method can be extended in a number of directions. Obviously, the method can be used to study scattering problems in multi-layered media with local perturbations, embedded obstacles, and penetrable structures. Besides scattering problems, the method can also be used to study eigenvalue problems, such as the problem for guided modes in open waveguide structures. We are planning to address these problems in our future works.

Acknowledgements. We would like to thank the two anonymous referees for their helpful comments.

REFERENCES

[1] B. K. Alpert. Hybrid Gauss-trapezoidal quadrature rules. *SIAM Journal on Scientific Computing*, 20(5):1551–1584, 1999.

[2] T. Arens and T. Hohage. On radiation conditions for rough surface scattering problems. *SIAM Journal on Applied Mathematics*, 70:839–847, 2005.

[3] J.-P. Berenger. A perfectly matched layer for the absorption of electromagnetic waves. *Journal of Computational Physics*, 114(2):185 – 200, 1994.

[4] O. P. Bruno and B. Delourme. Rapidly convergent two-dimensional quasi-periodic Green function throughout the spectrum including wood anomalies. *Journal of Computational Physics*, 262:262 – 290, 2014.

[5] O. P. Bruno, M. Lyon, C. Pérez-Arancibia, and C. Turc. Windowed Green function method for layered-media scattering. *SIAM Journal on Applied Mathematics*, 76(5):1871–1898, 2016.

[6] W. Cai. Algorithmic issues for electromagnetic scattering in layered media: Green's functions, current basis, and fast solver. *Advances in Computational Mathematics*, 16(2):157–174, 2002.

[7] W. Cai. *Computational Methods for Electromagnetic Phenomena*. Cambridge University Press, New York, NY, 2013.

[8] W. Cai and T. J. Yu. Fast calculations of dyadic Green's functions for Electromagnetic scattering in a multiplayered medium. *J. Comput. Phys.*, 5(5):247–251, 2000.

[9] S. N. Chandler-Wilde and B. Zhang. A uniqueness result for scattering by infinite rough surfaces. *SIAM Journal on Applied Mathematics*, 58:1774–1790, 1998.

[10] Z. Chen and X. Xiang. A source transfer domain decomposition method for Helmholtz equations in unbounded domain. *SIAM Journal on Numerical Analysis*, 51(4):2331–2356, 2013.

[11] W. C. Chew. *Waves and fields in inhomogeneous media*. IEEE PRESS, New York, 1995.

[12] W. C. Chew and W. H. Weedon. A 3D perfectly matched medium for modified Maxwell's equations with stretched coordinates. *Microwave and Optical Technology Letters*, 7(13):599–604, 1994.

[13] D. Colton and R. Kress. *Inverse Acoustic and Electromagnetic Scattering Theory (3rd Edition)*. Springer, 2013.

[14] T.J. Cui and W.C. Chew. Efficient evaluation of Sommerfeld integrals for TM wave scattering by buried objects. *Journal of Electromagnetic Waves and Applications*, 12(5):607–657,

1998.
[15] T.J. Cui and W.C. Chew. Fast evaluation of Sommerfeld integrals for EM scattering and radiation by three-dimensional buried objects. *IEEE Transactions on Geoscience and Remote Sensing*, 37(2):887–900, Mar 1999.
[16] V. Dominguez, M. Lyon, and C. Turc. Well-posed boundary integral equation formulations and Nyström discretizations for the solution of Helmholtz transmission problems in two-dimensional Lipschitz domains. *J. Integral Equations Applications*, 28(3):395–440, 2016.
[17] DeSanto J. and P. A. Martin. On the derivation of boundary integral equations for scattering by an infinite one-dimensional rough surface. *J. Acoust. Soc. Am.*, 102(1):67–77, 1997.
[18] R. Kress. A Nyström method for boundary integral equations in domains with corners. *Numer. Math.*, 58:145–161, 1990.
[19] R. Kress. *Linear Integral Equations (3rd Edition)*. Springer, 2014.
[20] J. Lai, L. Greengard, and M. OŃeil. A new hybrid integral representation for frequency domain scattering in layered media. *submitted*, arXiv:1507.04445v2, 2015.
[21] Matti Lassas and Erkki Somersalo. Analysis of the PML equations in general convex geometry. *Proceedings of the Royal Society of Edinburgh: Section A Mathematics*, 131(5):1183–1207, 2001.
[22] W. Lu and Y. Y. Lu. Efficient high order waveguide mode solvers based on boundary integral equations. *Journal of Computational Physics*, 272:507 – 525, 2014.
[23] W. McLean. *Strongly Elliptic Systems and Boundary Integral Equations*. Cambridge University Press, 2000.
[24] A. Meier and S. N. Chandler-Wilde. On the stability and convergence of the finite section method for integral equation formulations of rough surface scattering. *Mathematical Methods in the Applied Sciences*, 24(4):209–232, 2001.
[25] D. Miret, G. Soriano, and M. Saillard. Rigorous simulations of microwave scattering from finite conductivity two-dimensional sea surfaces at low grazing angles. *IEEE Transactions on Geoscience and Remote Sensing*, 52(6):3150–3158, June 2014.
[26] P. Monk. *Finite Element Methods for Maxwell's Equations*. Oxford University Press, 2003.
[27] J. A. Monro. *A super-algebraically convergent, windowing-based approach to the evaluation of scattering from periodic rough surfaces*. Dissertation (Ph.D.), California Institute of Technology., 2008.
[28] M. Ochmann. The complex equivalent source method for sound propagation over an impedance plane. *The Journal of the Acoustical Society of America*, 116(6):3304–3311, 2004.
[29] V. I. Okhmatovski and A. C. Cangellaris. Evaluation of layered media Green's functions via rational function fitting. *IEEE Microwave and Wireless Components Letters*, 14(1):22–24, Jan 2004.
[30] M. Paulus, P. Gay-Balmaz, and O. J. F. Martin. Accurate and efficient computation of the Green's tensor for stratified media. *Phys. Rev. E*, 62:5797–5807, Oct 2000.
[31] C. Pérez-Arancibia and O. P. Bruno. High-order integral equation methods for problems of scattering by bumps and cavities on half-planes. *J. Opt. Soc. Am. A*, 31(8):1738–1746, Aug 2014.
[32] Balth Van Der Pol. Theory of the reflection of the light from a point source by a finitely conducting flat mirror, with an application to radiotelegraphy. *Physica*, 2(1):843 – 853, 1935.
[33] M. Saillard and G. Soriano. Rough surface scattering at low-grazing incidence: A dedicated model. *Radio Science*, 46(5):n/a–n/a, 2011. RS0E13.
[34] A. Sommerfeld. ber die ausbreitung der wellen in der drahtlosen telegraphie. *Annalen der Physik*, 333(4):665–736, 1909.
[35] P. Spiga, G. Soriano, and M. Saillard. Scattering of electromagnetic waves from rough surfaces: A boundary integral method for low-grazing angles. *IEEE Transactions on Antennas and Propagation*, 56(7):2043–2050, July 2008.
[36] G. Taraldsen. The complex image method. *Wave Motion*, 43(1):91 – 97, 2005.
[37] D. J. Thomson and J. T. Weaver. The complex image approximation for induction in a multi-layered earth. *Journal of Geophysical Research*, 80(1):123–129, 1975.
[38] L. N. Trefethen. *Spectral Methods in MATLAB*. SIAM, 2000.
[39] H. Weyl. Ausbreitung elektromagnetischer wellen ber einem ebenen leiter. *Annalen der Physik*, 365(21):481–500, 1919.
[40] Z. Zhao, L. Li, J. Smith, and L. Carin. Analysis of scattering from very large three-dimensional rough surfaces using mlfmm and ray-based analyses. *IEEE Antennas and Propagation Magazine*, 47(3):20–30, June 2005.